

Analysis of texture evolution in magnesium during equal channel angular extrusion

Benoît Beausir^{a,b}, Satyam Suwas^c, László S. Tóth^{a,*}, Kenneth W. Neale^b,
Jean-Jacques Fundenberger^d

^a *Laboratoire de Physique et Mécanique des Matériaux, Université de Metz, Ile du Saulcy, 57045 Metz Cedex 1, France*

^b *Faculty of Engineering, Université de Sherbrooke, Sherbrooke, Québec, Canada J1K 2R1*

^c *Department of Materials Engineering, Indian Institute of Science, Bangalore 560 012, India*

^d *Laboratoire d'Etude des Textures et Application aux Matériaux, Université de Metz, Ile du Saulcy, 57045 Metz Cedex 1, France*

Received 13 May 2007; received in revised form 3 September 2007; accepted 8 September 2007

Available online 19 November 2007

Abstract

Texture development in magnesium during equal channel angular extrusion (ECAE) with an angle of 90° between the intersecting channels has been studied. Textures were simulated using polycrystal plasticity models as well as determined experimentally for routes A, B_c and C up to four passes. Based on a previous study on texture evolution during the simple shear of materials with hexagonal crystal structures [Beausir B, Tóth LS, Neale KW. *Acta Mater* 2007;2695:2705], the ideal orientations for ECAE of hexagonal metals were identified considering the shear to be at the 45° intersection plane of the two channels. Although dynamic recrystallization (DRX) was experimentally observed during the ECAE experiments, the polycrystal modeling using the viscoplastic self-consistent (VPSC) model was able to reproduce the experimental textures successfully. This was attributed to the fact that the textures were c-type fibers with their axis of rotation parallel to the c-axis, whereas the nucleation of grains during DRX takes place in positions simply rotated around the c-axis. © 2007 Published by Elsevier Ltd on behalf of Acta Materialia Inc.

Keywords: Equal channel angular extrusion; Magnesium; Ideal orientations; Texture; Crystal plasticity

1. Introduction

Magnesium and its alloys, due to their having the lowest density amongst the structural materials, are potential candidate materials for structural components in automotive industries. Due to a significant reduction in weight, there are many associated advantages, for example lower fuel consumption and therefore lowering of the pollution level. However, the forming of components from magnesium is relatively difficult due to its limited ductility, which is essentially attributed to the limited number of slip systems owing to its hexagonal crystal structure. Various solutions have been proposed to overcome this problem. One possi-

bility is to employ the equal channel angular extrusion (ECAE) process, where the deformation mode is near simple shear, which requires fewer slip systems near the ideal components than in other processes. It also leads to a large grain refinement without significant dimension changes of the sample. The ECAE process consists of extruding a lubricated sample through two channels of equal and identical area of cross-section. The process can be repeated multiple-times; there is no change in area of cross-section due to the process. There are two important attributes of this progression: (i) large deformations being able to harden the material until its theoretical limit and (ii) the development of an ultra-fine microstructure.

The ECAE process is characterized by the development of characteristic deformation textures [1–7]. Moreover, plastic deformation of magnesium and its alloys is strongly affected by the crystallographic texture [7,8]. The

* Corresponding author. Tel.: +33 387 547 238; fax: +33 387 315 366.
E-mail address: toth@univ-metz.fr (L.S. Tóth).

deformation texture can be retained even after subsequent heat treatment and can significantly enhance formability [2]. Even superplastic behavior can be achieved in ECAE-treated magnesium alloys [9,10]. Fatigue life is also extended [11]. The improvements in the mechanical characteristics of ECAE-deformed pure Mg and its alloys make the ECAE process attractive for engineering applications [12]. It is therefore highly desirable to improve our understanding of the evolution of anisotropy in ECAE. In this respect, there are some important issues not yet resolved. One is the documentation of the ideal textures that can develop in ECAE, namely the characterization of the ideal orientations and fibers and the interpretation of their evolution. This will be done in the present paper using the results of a previous analysis carried out for simple shear [13]. Another important issue is the contribution of the different deformation mechanisms to the total deformation (basal, prismatic, pyramidal slip and twinning). Information on that can be obtained by elaborate experimental means [5], or by large strain deformation texture simulations compared to experiments. In order to avoid twinning, the ECAE process is usually applied above 200 °C on Mg, although recent tests carried out in a 135° die were successful even at room temperature [9].

This paper provides a theoretical study of texture evolution during the ECAE process, validated by experiments. Simulations have been performed using the viscoplastic polycrystal self-consistent model (VPSC). Experiments were carried out following the three important routes of ECAE, namely A, B_c and C up to four passes in a 90° die at 250 °C. Finally, the characteristics of the textures so obtained with respect to ideal orientations of hcp materials in simple shear have been examined.

2. The ideal orientations of Mg in a 90° ECAE die

It is commonly accepted that the deformation process during ECAE can be well approximated by simple shear acting at the intersection plan of the two channels that form the die [14]. Although deviations exist from this so-called simple shear model (see the flow line model of Tóth et al. [15] and the FAN model of Beyerlein and Tomé [16]), it remains a good approximation in many practical cases. The main effects caused by the deviations from simple shear are some tilts of the ideal components from their ideal positions, which can be reproduced with the above-cited models [15,16]. In the present study, the simple shear model was employed to simulate texture development during ECAE.

As the deformation mode is considered to be simple shear, the ideal orientations are the same in ECAE, except that the reference system is rotated by 45° in the positive rotation direction around the TD axis, as illustrated in Fig. 2. As the texture is examined in the non-rotated (1,2,3) reference system, the ideal positions move by 45° in the positive ϕ_1 direction. The ideal positions for simple shear of hexagonal crystals were identified in a recent work

Table 1
Ideal orientations for hexagonal materials during ECAE

Fibre	ϕ_1 (°)	ϕ_2 (°)	ϕ_3 (°)
B	45	90	0–60
P	45	0–90	30
Y	45	30	0–60
C ₁	105	90	0–60
C ₂	165	90	0–60

[13]; they are all fibers. Their positions in the laboratory reference system are given in Table 1. They are also depicted in (0002) and (10 $\bar{1}$ 0) pole figures in Fig. 3. These key figures can be used in the characterization of the measured textures. Among the five fibers, it is the B and P that are the most significant.

3. Experimental details

Magnesium of 99.9% purity was obtained in a hot-forged condition. The initial grain size of the material was ~ 200 μm . Billets extracted from the forged plate were subjected to ECAE at 250 °C up to four passes following the routes A, B_c and C. The experiments were carried out using a specially designed die [17] with an angle $\Phi = 90^\circ$ between the two channels of square cross-section (10 \times 10 mm) without any rounding of the corners (Fig. 1). The pressing speed was 1 mm min⁻¹. In each route, the sample had to be turned by +90° around the TD axis in order to position the deformed sample back into the die. In routes B_c and C, there were additional rotations, around the specimen axis by +90° and +180°, respectively. Textures were measured on the top surface of the bottom half of the sample by X-ray diffraction in (0002), (10 $\bar{1}$ 0), (0002), (10 $\bar{1}$ 1), (10 $\bar{1}$ 2), (11 $\bar{2}$ 0) and (10 $\bar{1}$ 3) pole figures. The microstructures were investigated by the electron back-scatter diffraction (EBSD) technique on the TD plane using a FEI–Sirion field emission gun scanning

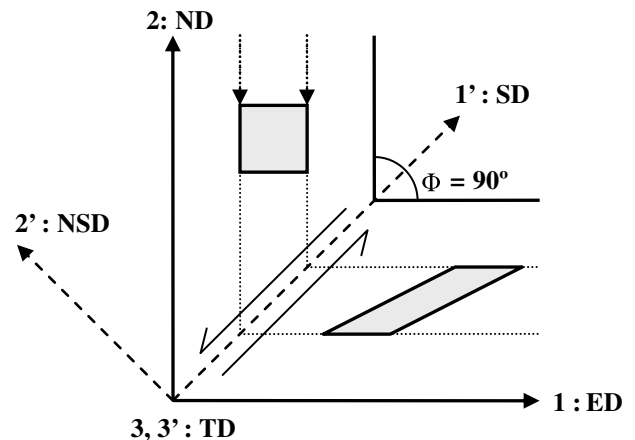


Fig. 1. Reference systems used in the ECAE process showing the deformation of a square by simple shear at the intersection plane of the channels.

electron microscope (FEG-SEM) with a step size of 1.0 μm . The data acquisition and analyses were performed using TSL software.

4. Experimental textures and microstructures

From the six measured incomplete pole figures, the harmonic coefficients of the orientation distribution function (ODF) were calculated. These coefficients were then expressed in the reference frame (ED, ND, TD) indicated in Fig. 1, which corresponds to the (x_1, x_2, x_3) Cartesian frame used for the definition of the Euler angles. (See also Fig. 2 for the laboratory reference system.) From the ODFs, complete pole figures were calculated and are presented in Figs. 4–6. For each pass, the input texture is the output experimental texture of the previous pass, rotated with respect to the considered route.

The initial texture presents a relatively strong (0002) fiber, with the fiber axis parallel to the ED direction when the sample is placed into the vertical channel. This texture originates from the previous rolling process of the produced Mg plate. After one pass, the texture seems to be just simply rotated around the TD axis in the positive rotation direction by $\sim 105^\circ$. It approaches the B fiber position but does not reach it. A split of the fiber can also be identified in the (0002) pole figure. This texture has to be rotated by -90° around TD to position the sample back into the die for the second pass in route A. The pole figures thus obtained are also shown in Fig. 4 and are referred to as “input texture”. As can be seen, this texture before the second pass is very much similar to the texture before the first pass; it only differs from it by a rotation of $\sim 15^\circ$ around the TD axis. During the second pass, the texture rotates somewhat less than in the first pass, about $+90^\circ$ around TD. It cannot reach the B fiber position again. These rotations are then repeated in the third and fourth passes in route A ECAE. Thus, the texture after each ECAE pass is nearly

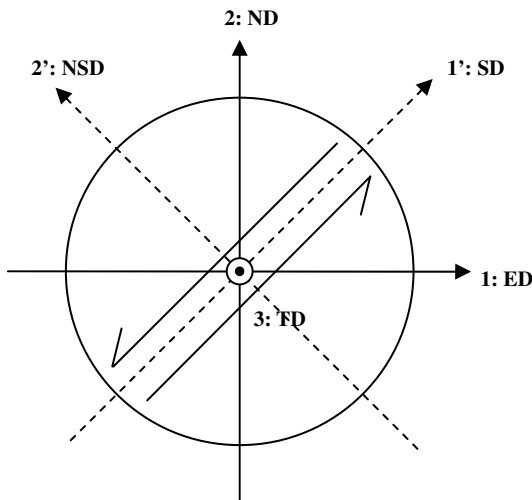


Fig. 2. Reference systems used in the pole figures.

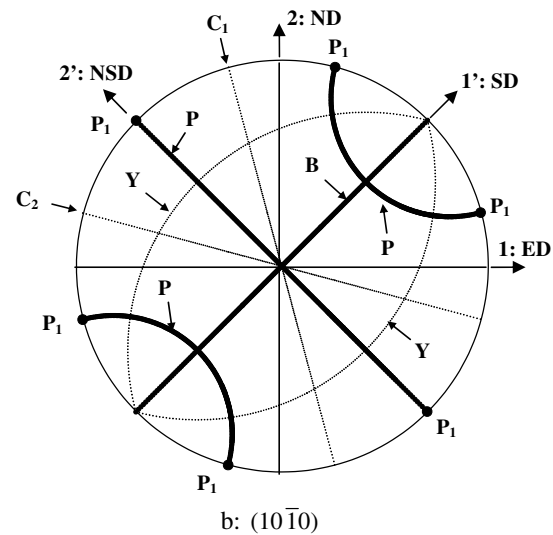
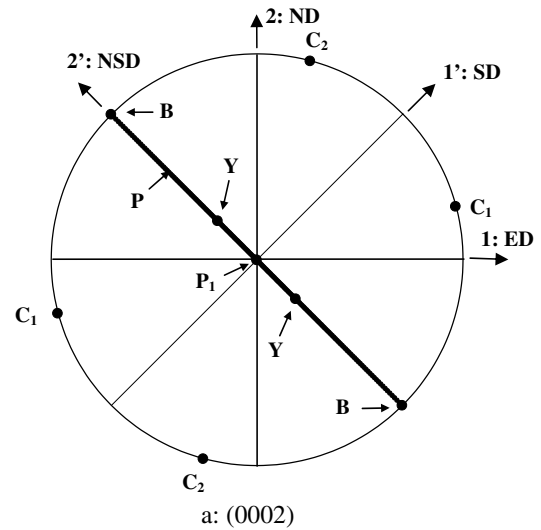


Fig. 3. The locations of the ideal fibers in ECAE textures of magnesium under simple shear loading on: (a) (0002) and (b) $(10\bar{1}0)$ pole figures. The main fibers are identified with thick lines.

the same. This peculiarity of the texture development in route A ECAE of Mg will be fully explained in the simulation part of the present paper using the rotation field characteristics of simple shear.

The texture development in route B_c deformation is quite similar to that in route A (see Fig. 5). There is, however, a systematic difference, clearly visible in both the (0002) and $(10\bar{1}0)$ pole figures; namely the B fiber develops in a slightly rotated position around an axis which lies in the 45° oriented intersection plane of the die, the 1' axis in Fig. 2, which is the simple shear direction axis. The rotation is $\sim 20^\circ$ in the positive sense. When the position of the obtained fiber is compared to the position of the fiber before each pass, one can see that the deformation texture can be obtained from the initial texture by a rotation of about -45° again around the direction given by the simple shear direction.

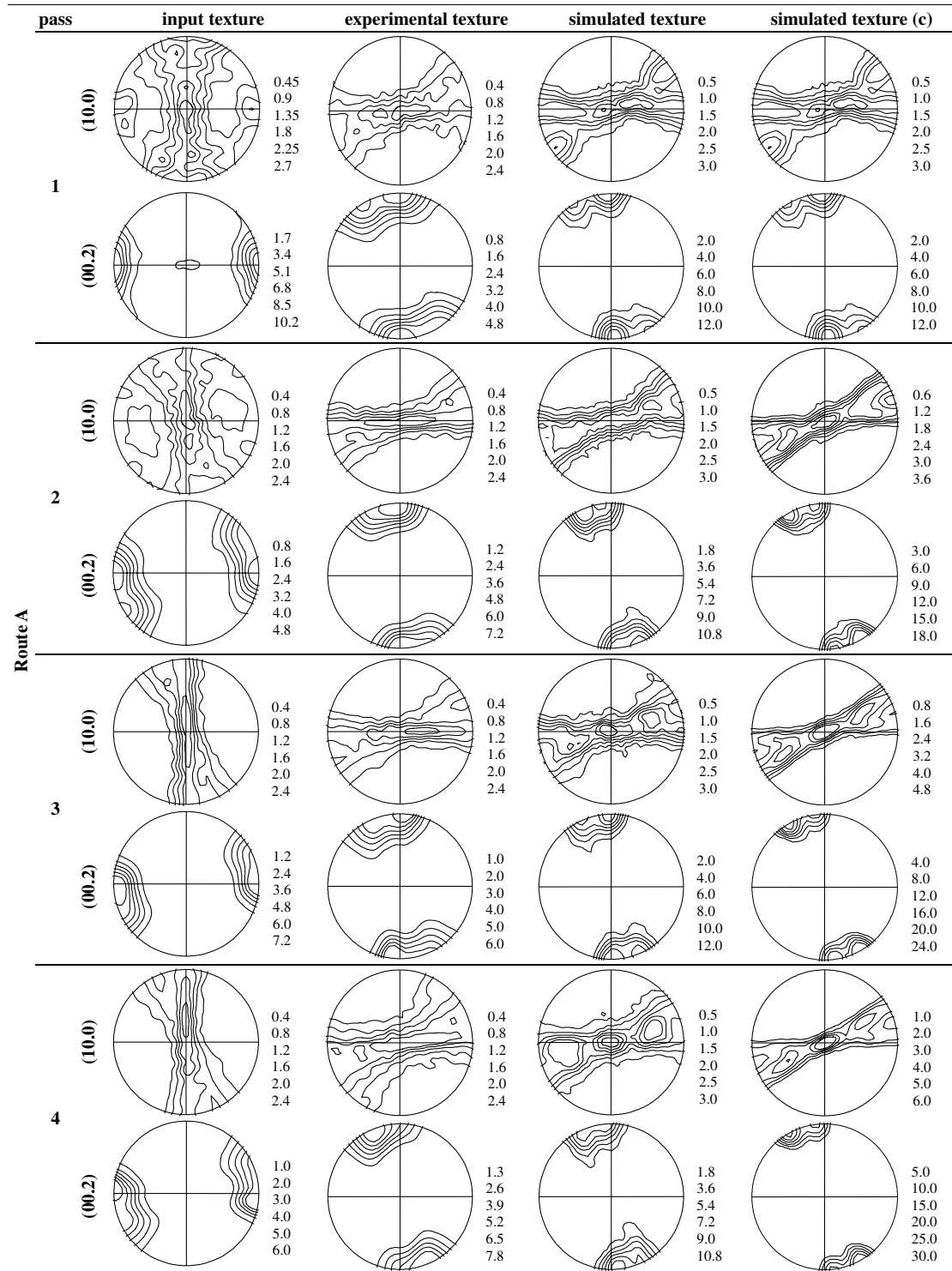


Fig. 4. Experimental and simulated textures of magnesium in route A of ECAE.

The experimental textures for route C processed materials are presented in Fig. 6. As can be seen, before the second pass begins, the texture is not too far from the very initial texture that is the input texture of the first pass. This peculiarity is due to the special texture developing in the first pass; the first-pass deformed texture is just a 105° TD rotated version of the initial texture. That rotation is

not far from 90°, so by rotating it about ED by 180° and then about TD by 90°, one obtains a texture that is similar to the very initial one. Nevertheless, there are some differences, which are well visible by comparing (0002) and (10 $\bar{1}$ 0) pole figures of the initial texture and the input texture of route C, pass 2. Actually, because the initial fiber is rotated to the right by ~15°, after pass 2, the fiber

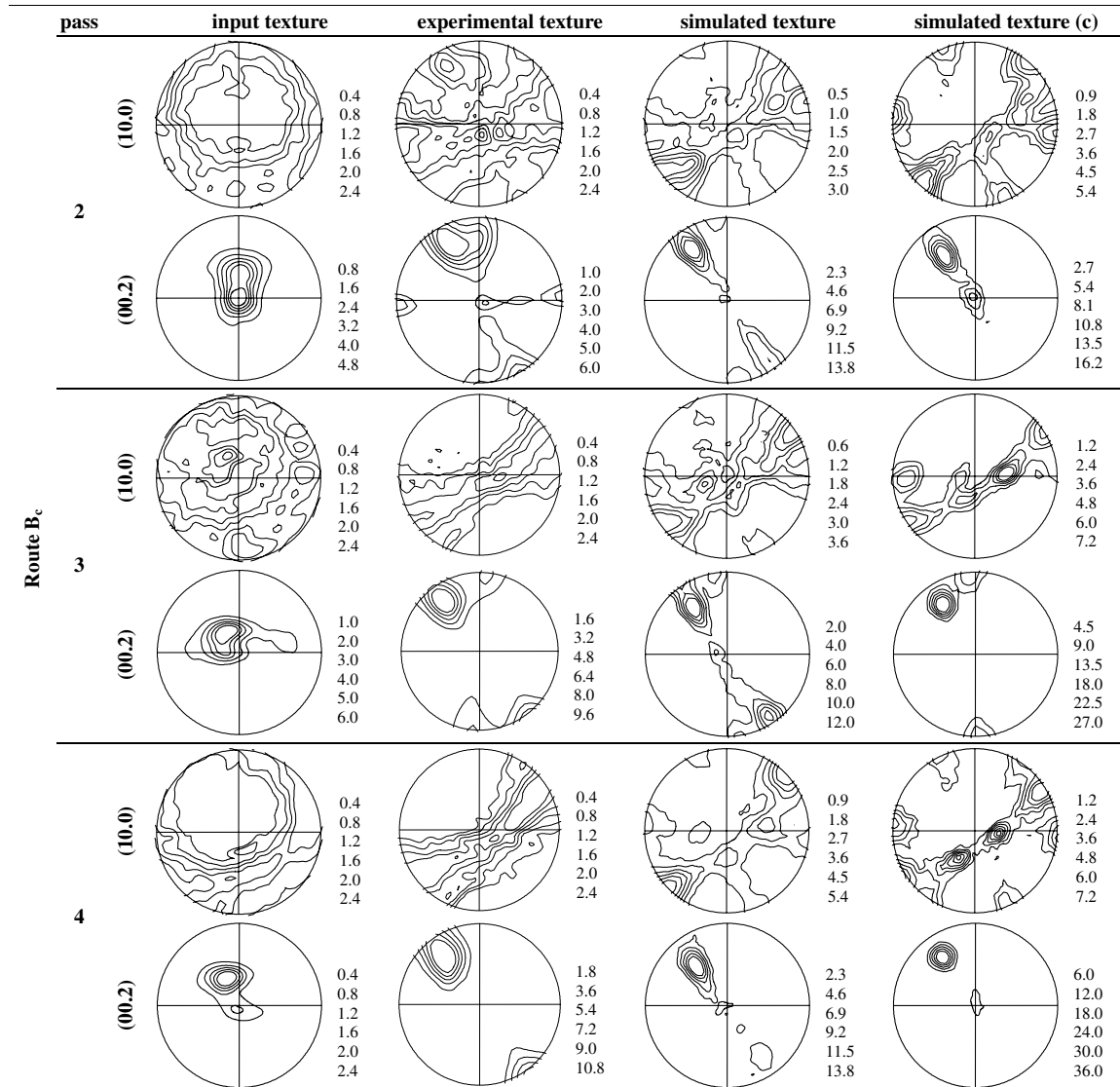


Fig. 5. Experimental and simulated textures of magnesium in route B_c of ECAE.

approaches the ideal position to a closer extent. At larger pass numbers, one can observe two maxima in the (0002) pole figures; best visible after pass three. In general, apart from the double peak, which can be quite strong, the texture is quite similar after each pass in route C, too.

The EBSD results are presented in Fig. 7 for the samples deformed in route A to one pass, (hereafter referred to as A1), in route B_c (for the first B_c pass, B2) and in route C (for the first C pass, C2). The color code corresponds to the orientation of the TD axis with respect to the crystal reference system. As can be seen, the grain size decreased drastically; for each of the samples it is ~20 μm (one-tenth of the initial). There is, however, a bimodal character of the microstructure with some significantly larger grains present in the samples. Their population is less significant in the second passes (C2 and B2). The micrographs in Fig. 7 show clear evidences of dynamic recrystallization (DRX). One reason is the grain shape that is nearly spherical, which

should be very much elongated due to large shear in the ECAE test. Also, the forms of the grains, that are not always convex, are clear indications of the occurrence of DRX.

5. Texture simulation conditions

According to the simple shear model of ECAE, the velocity gradient of simple shear in the plane of symmetry ($1', 2', 3'$ reference system in Fig. 2) is given by:

$$L = \begin{pmatrix} 0 & -\dot{\gamma} & 0 \\ 0 & 0 & 0 \\ 0 & 0 & 0 \end{pmatrix}_{1',2',3'} \quad (1)$$

Here, $\dot{\gamma}$ is positive, meaning that the shear direction is negative. When this velocity gradient is expressed in the ECAE reference system (1,2,3), it transforms to:

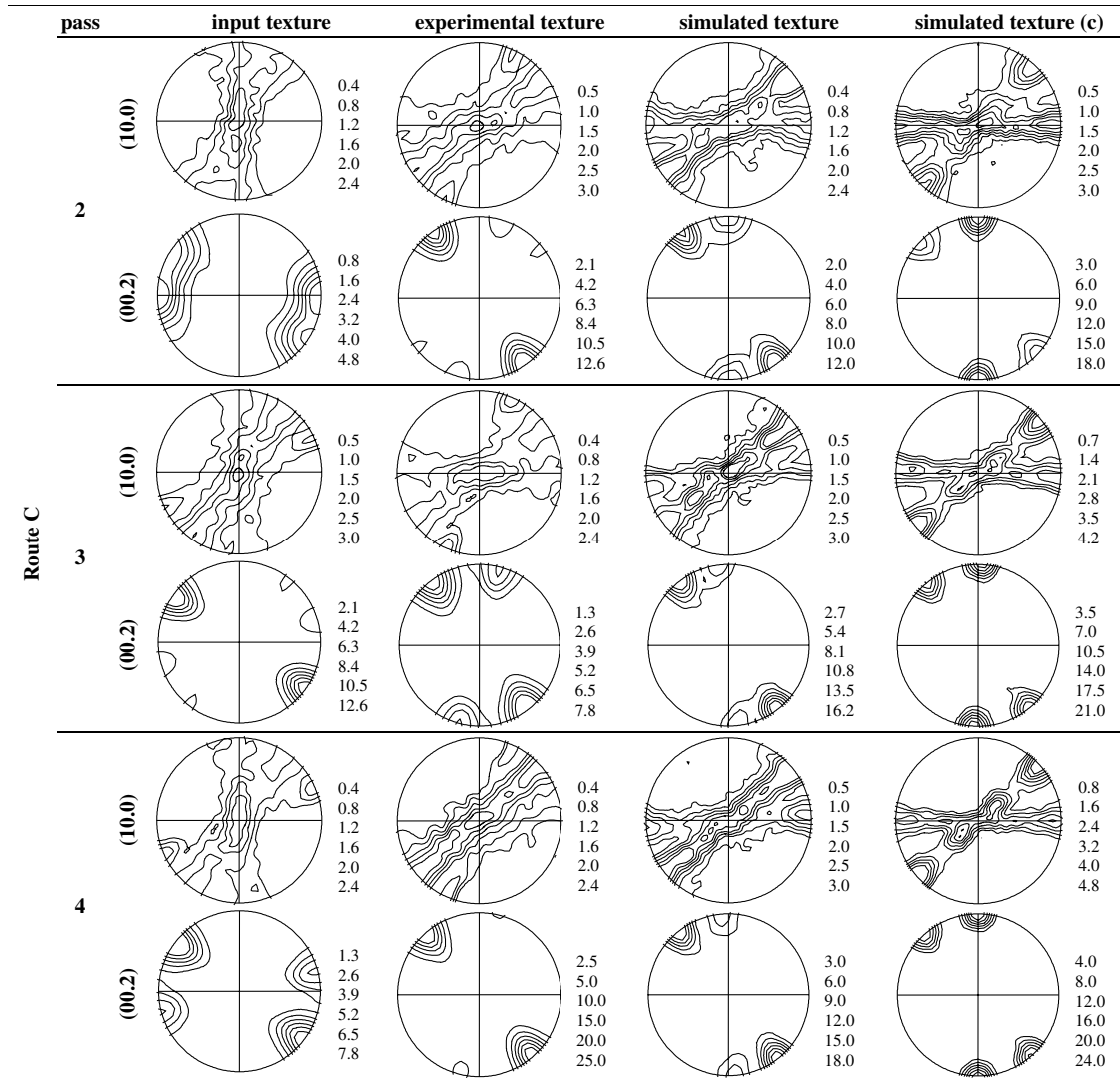


Fig. 6. Experimental and simulated textures of magnesium in route C of ECAE.

$$L = \frac{\dot{\gamma}}{2} \begin{pmatrix} 1 & -1 & 0 \\ 1 & -1 & 0 \\ 0 & 0 & 0 \end{pmatrix}_{1,2,3} \quad (2)$$

As can be seen from this second expression, the velocity gradient describes tension in the extrusion direction (1 = ED), compression in the normal direction (2 = ND) and a pure rigid-body rotation around the TD axis (3 = TD) [15]. L can be readily incorporated into a polycrystal plasticity model up to a shear strain of $\gamma = 2$ in each pass.

Simulations have been carried out using the VPSC model. (The DRX observed in the experiments was not modeled in the polycrystal plasticity model. This could be justified a posteriori: see Section 6.) The non-incremental tangent-based VPSC model was employed in its isotropic version concerning the interaction between the matrix and the grain [18]. More precisely, the finite-element-tuned model was used where the scaling parameter was 0.6 [19].

For crystallographic slip, the rate-dependent plastic slip law was employed [20]:

$$\tau^{s,f} = \tau_0^f \text{sgn}(\dot{\gamma}^{s,f}) \left| \frac{\dot{\gamma}^{s,f}}{\dot{\gamma}_0} \right|^m = \tau_0^f \frac{\dot{\gamma}^{s,f}}{\dot{\gamma}_0} \left| \frac{\dot{\gamma}^{s,f}}{\dot{\gamma}_0} \right|^{m-1} \quad (3)$$

This constitutive law has been widely used in crystal plasticity simulations [21–24]. Here, $\tau^{s,f}$ is the resolved shear stress in the slip system indexed by “s” of the slip system family indexed by “f”, $\dot{\gamma}^{s,f}$ is the slip rate, the τ_0^f value is the reference stress level (at which the slip rate is $\dot{\gamma}_0$) and m is the strain rate sensitivity index. The reference shear rate $\dot{\gamma}_0$ is supposed to be constant for all slip systems. The slip systems are grouped into “families”. The index f is used to represent a particular family. The main slip families in hexagonal structures are the basal, prismatic and pyramidal slips. It is assumed here that the reference shear stress, τ_0^f , is the same for a given slip system family, but can be different from one family to another.

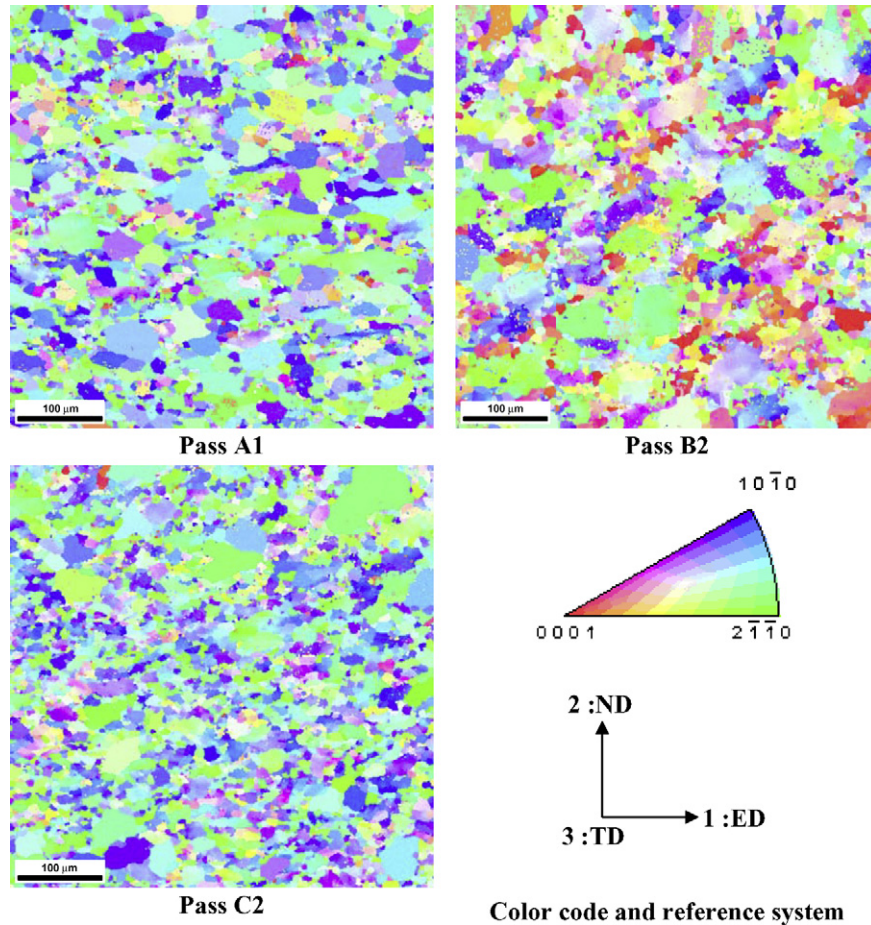


Fig. 7. EBSD maps obtained on the TD surface of the A1, C2 and B2 specimens. The colored triangle indicates the orientation of the TD axis in the hexagonal crystal reference system.

An important issue in hexagonal materials is the relative contribution of the different slip families. Agnew et al. [4] found that the best simulation results could be obtained using the following combination of the reference stresses:

$$\begin{aligned} \tau_0^{\text{basal}} &= 1; & \tau_0^{\text{prism.}} &= 8; & \tau_0^{\text{pyr.}(a)} &= 8; & \tau_0^{\text{pyr.}(c+a)/A} &= 6; \\ \tau_0^{\text{pyr.}(c+a)/B} &= 6. \end{aligned} \quad (4)$$

The same conclusion could be drawn from our simulations. The strain rate sensitivity, m , was chosen to be 0.2, which corresponds to the test temperature 250 °C (experiments report an m -value of 0.15 at 200 °C in AZ31 [1]). The initial texture was discretized into 2000 grain orientations and was used as input in the first pass. Hardening was not taken into account. Two types of simulations were carried out:

1. in the so-called “continuous” technique (indexed as “c” in the last columns in Figs. 4–6), in each subsequent pass the previously simulated texture was the input texture;
2. in the “texture-corrected” technique, in each pass the experimental previous texture was discretized and used in the new pass.

The output 2000 discrete orientations were converted into a continuous ODF for the presentation of the defor-

mation textures. For this purpose, a 5° Gaussian spread was used around each orientation, then the harmonic coefficients of the distribution were derived up to a rank of $L = 34$. (Actually, the value of the Gaussian spread depends inversely on the number of grains used in a simulation. In a real measurement, the grain number is usually much higher compared to the simulation; this is why relatively large values need to be used to generate a continuous ODF from discrete orientations.) The results of the simulations are presented in Figs. 4–6.

6. Discussion of the texture evolution

Although microstructural evidence clearly indicates that DRX took place in Mg during the present ECAE experiments, it will be shown below that the texture development was not affected by the DRX process. For the understanding of this situation, first the texture development will be discussed without taking into account DRX.

6.1. Characteristics of the rotation field

For a better understanding of the evolution of the texture during ECAE, it is useful to present the rotation

field and the divergence quantities in the appropriate orientation space. Such an analysis has been carried out for the case of simple shear in Ref. [13] and can be readily transposed for the ECAE process. It simply involves a shift of the rotation field and the divergence by 45° in the positive φ_1 direction. For completeness, we recall the definition of the “rotation field” and the divergence.

The rotation field can be well illustrated by displaying the lattice spin vector defined in orientation space: $\dot{g} = (\dot{\varphi}_1, \dot{\varphi}_2)$. It is obtained from the lattice spin Ω of the real laboratory space using the following relations [25,26]:

$$\begin{aligned}\dot{\varphi}_1 &= \Omega_{12} - \varphi_2 \cos \varphi, \\ \dot{\varphi} &= \Omega_{32} \cos \varphi_1 + \Omega_{13} \sin \varphi_1, \\ \dot{\varphi}_2 &= (\Omega_{32} \sin \varphi_1 - \Omega_{13} \cos \varphi_1) / \sin \varphi.\end{aligned}\quad (5)$$

The divergence quantity, $\text{div}(\dot{g})$, also gives useful information on the nature of the field. It is defined by

$$\text{div}(\dot{g}) = \frac{\partial \dot{\varphi}_1}{\partial \varphi_1} + \frac{\partial \dot{\varphi}}{\partial \varphi} + \frac{\partial \dot{\varphi}_2}{\partial \varphi_2}.\quad (6)$$

The rotation spin vector and the divergence quantity are displayed in Fig. 8 for the velocity gradient defined in Eq. (2) in the $\varphi_2 = 0^\circ$ and $\varphi_2 = 30^\circ$ sections. The locations of the ideal fibers are also indicated in the figure. For regions of high persistence of grain orientations, the lattice spin, \dot{g} , is small and the divergence is $\text{div}(\dot{g}) < 0$. These are the expected positions of the ideal texture components. They all manifest in the form of fibers and are listed in Table 1.

Deformation textures developing from a relatively strong initial texture are typically fiber textures (see Fig. 4). This initial texture is plotted in two ODF sections, as shown in Fig. 8. The fiber appears in the vicinity of the C1 fiber. The C1 position is just a saddle point with little persistence of the grain orientations [13]. The lattice rotation is towards the right, which corresponds to the increasing φ_1 angle, thus the initial texture is unstable with respect to the simple shear of ECAE. The texture rotates to the right by quite a large amount during the first-pass deformation itself (105°). This rotation is much larger than the rigid-body rotation, which amounts to only 57.3° during the shear of 2.0 that corresponds to the deformation of a material element in an ECAE die with a 90° angle according to the simple shear model of Segal [14]. Thus, the rotation of the texture is unusually high compared to the rotations observed in other crystal structures; for example, in cubic materials, where the rotations are much less [15,16]. The speed of texture evolution is a technologically important issue which must be understood to enable possible control of the texture. For this reason, a figure was prepared in which the ratio r of the lattice spin $\|\Omega\|$ with respect to the rigid-body spin $\|\beta\|$ is plotted: $r = \|\Omega\|/\|\beta\|$ for an m -value of 0.2 (see Fig. 9). We recall that the lattice spin is the difference between the rigid-body spin and the plastic spin ω :

$$\Omega = \beta - \omega.\quad (7)$$

β is a constant value during the shear process, while ω depends on the crystal orientation; ω can even be opposite or equal to β . The case when they are equal leads to the stable orientations in shear for rate-insensitive slip. However, in the case when they are opposite, the lattice spin becomes twice the rigid-body spin, a case which has not yet been studied analytically in a general way, to the knowledge of the authors. Actually, as can be seen in Fig. 9, r varies between about 0 and 2. It is small in the vicinity of the ideal fibers B and P, but in most volumes of Euler space, it is >1 . That is, the lattice rotation in general is larger than the rigid-body spin in a large interval in the ODF to the right of the initial fiber. This is the reason why the texture can rotate much more than the rigid-body rotation.

The Appendix presents a detailed analysis regarding the slip distribution and the nature of the operating slip systems along the B fiber, as well as along the 90° φ_1 rotated B fiber line for the case of simple shear. The results are the same for the present ECAE test, by simply adding 45° to the φ_1 angle. Along the ideal B fiber, there are two active basal slip systems that accommodate the prescribed simple shear and r is zero for strain-rate-insensitive slip. The plastic spin is equal to the rigid-body spin along the B fiber in the strain-rate-insensitive case. This result remains qualitatively the same for the present ECAE simulations carried out for $m = 0.2$. To the right from the ideal B fiber, on the line of $\varphi_1 = 90^\circ$ in the ODF, the r -value increases nearly up to 2 (in the $m = 0$ case it is exactly 2), which represents a very fast lattice rotation. This position ($\varphi_1 = 135^\circ$) is particular. One can see from Eq. (7) that an r value of 2 should correspond to a plastic spin that is now in the same direction as the rigid-body spin. It is shown in the Appendix that this prevails all along the 90° φ_1 rotated B fiber, i.e. the lattice rotation is twice as high as the rigid-body spin. For the above reasons, the texture can readily rotate more than the imposed rigid-body rotation, which is $\sim 105^\circ$ instead of 57.3° . However, even this large rotation is not enough to reach the ideal position because the B fiber is at 135° distance from the initial fiber (see Fig. 8a). Another interesting feature of the experimental texture is an apparent split of the fiber showing two maxima, well visible in the (0002) pole figure after the first pass. Actually, a similar split already exists in the initial texture; it is well visible in the two ODF sections of the initial texture in Fig. 8a and b. After the pass, that split is nearly the same, both in the experiment and in the simulations. Thus, the apparent split is attributed to the initial texture.

6.2. Route A textures

The textures that develop in further passes in route A can be interpreted as follows. For a new ECAE pass in route A, the sample has to be rotated by -90° around the TD axis. Such a rotation involves a displacement of

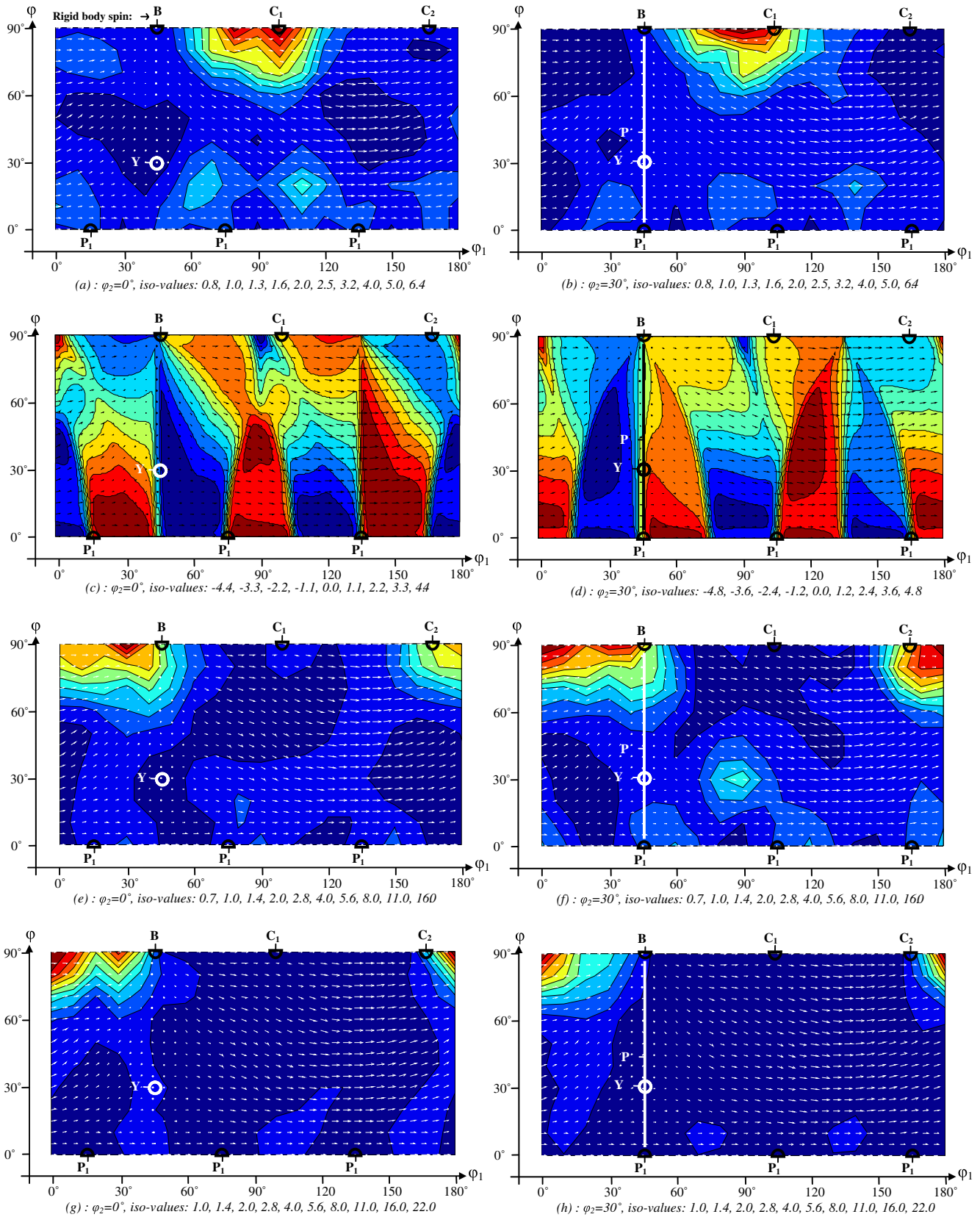


Fig. 8. Texture evolutions during the first pass of the route A: (a) and (b) show the ODF of the input texture; (c) and (d) present the lattice rotation fields (\dot{g}) and divergences ($\text{div}(\dot{g})$) associated with the ECAE test for the set of relative reference stresses [1,8,8,6,6] and the strain rate sensitivity $m = 0.2$; (e) and (f) show the ODF of the experimental texture after pass one; (g) and (h) display the ODF of the simulated texture after one pass. (a), (c), (e) and (g) are the ODF section at $\varphi_2 = 0^\circ$, while (b), (d), (f) and (h) are the ODF section at $\varphi_2 = 30^\circ$ constant.

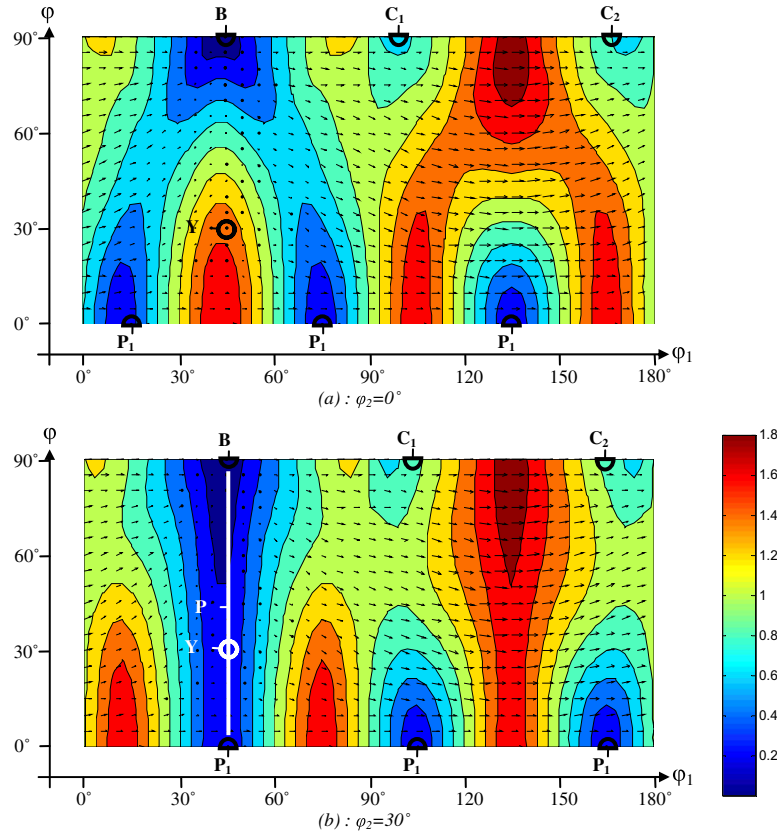


Fig. 9. The ratio of the lattice spin to the rigid-body spin $r = \|\Omega\|/\|\beta\|$, (a) and (b) in $\phi_2 = 0^\circ$ and $\phi_2 = 30^\circ$ ODF sections, respectively ($m = 0.2$).

the whole texture by -90° along the ϕ_1 -axis in Euler space (the laboratory reference system is always kept the same). Thus, the whole fiber is shifted back to nearly the same position as it was before the first pass; not exactly though, as 90° is less than the rotation of the fiber due to deformation by 105° . In the second and subsequent passes, the texture rotates as much due to strain as it does due to the sample re-positioning (see Fig. 4). This is the reason why the texture seems to be nearly the same after each pass.

6.3. Route B_c textures

The route B_c textures are different from those in routes A and C. As was shown in Section 4, the deformation texture can be derived from the initial texture by a rotation of about -45° around the shear direction (which lies at 45° with respect to the die axis in the intersection plane of the channels). This situation is repeated in each pass and nearly the same texture appears after each B_c pass. In order to understand the evolution of the texture in route B_c , the textures just before and after the fourth pass are displayed in ODF form in Fig. 10. Only the $\phi_2 = 30^\circ$ section is displayed, as the texture is almost the same in all the other $\phi_2 = \text{constant}$ sections. As can be seen in Fig. 10, the initial fiber is located in an area from where the rotation field will drift it in the direction of the B fiber; along a trajectory that is nearly parallel to the B fiber. The B fiber cannot be

reached during the plastic strain of the ECAE deformation pass as the lattice rotation is small in this region. It is also important to note that in route B_c deformation there is no sample symmetry in the ODF (a monoclinic symmetry could be used in routes A and C for the presentation of the textures in the ODF space); this is why the ϕ_1 angle ranges up to 360° in Fig. 10. In conclusion, while large lattice rotations take place in route A passes around the TD axis (also in route C, see below), route B_c is distinct as the texture rotates by a much smaller amount and not around the TD axis.

6.4. Route C textures

Concerning the texture evolution in route C, although it seems to be rather similar to route A, there are some additional features in the textures that can be readily interpreted with the help of the rotation field and the persistence characteristics of the ECAE process. One can see that the additional rotation of 180° around the sample axis, which it is necessary to apply in route C, leads to an initial texture that is rotated by about -30° along the ϕ_1 -axis of Euler space with respect to the route A texture before pass two (cf. the corresponding pole figures in Figs. 4 and 6). In this way, as the initial fiber is quite wide, some part of the fiber already lies in a high persistence zone of the B fiber; thus it will rotate very little during the first

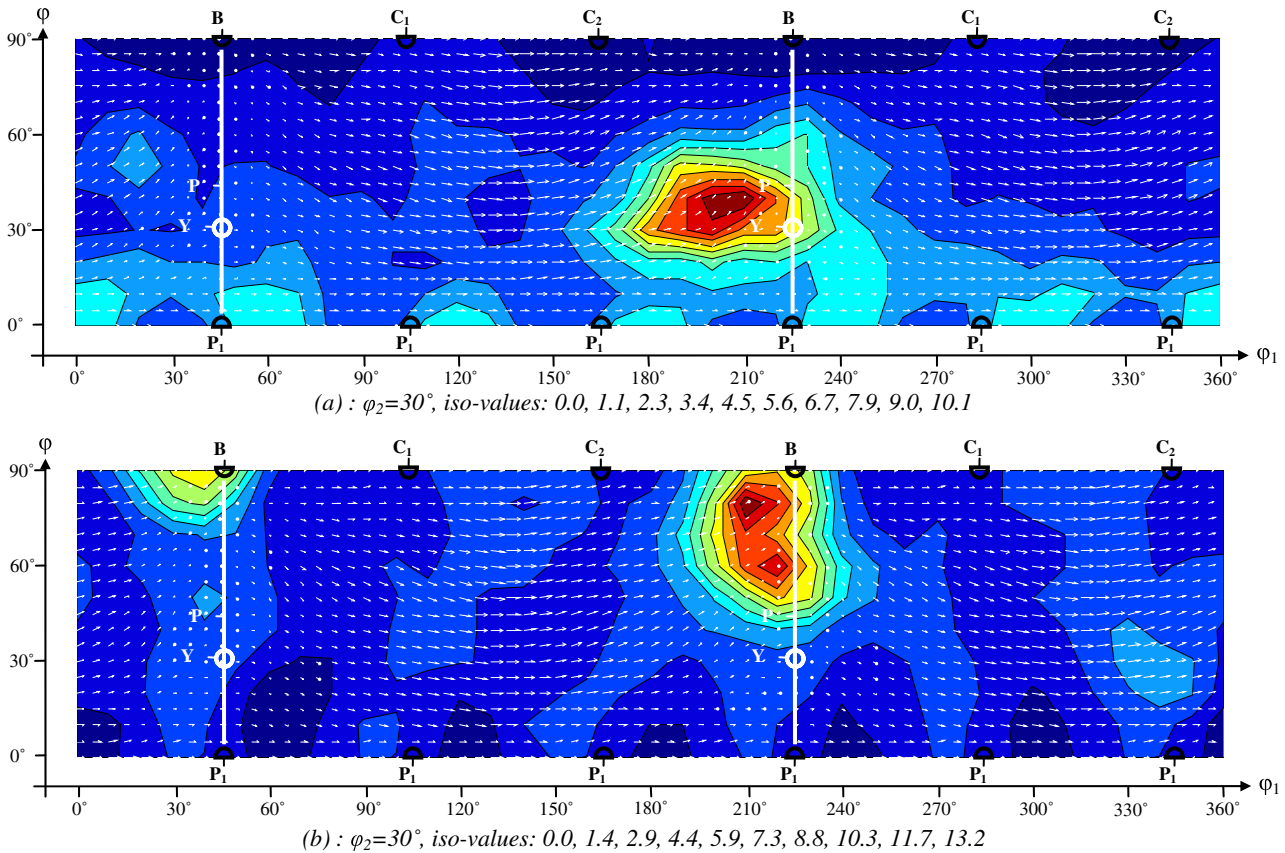


Fig. 10. Texture evolution during the fourth pass of route Bc in the $\phi_2 = 30^\circ$ ODF sections: (a) input texture; (b) texture after the pass.

route C pass. A larger part of the initial fiber, however, is in the zone of positive divergence (to the right from the B fiber position in Fig. 8c and d) performing a fast rotation of the texture. For the reasons explained above and in the Appendix, this component, although it rotates more than the rigid-body rotation, cannot reach the B fiber. The result is the formation of a double peak in the pole figures. In the first pass, the peak corresponding to the initial B fiber is quite weak. However, the same process is repeated in the next route C pass which leads to high intensities for both peaks. Finally, in the last pass of route C, the same situation is valid as in the first route C pass. This is due to the well-known fact that in every second pass, the same shear is applied on the texture in route C.

6.5. Dynamic recrystallization

The colors of the grains in the EBSD maps (Fig. 6) are in good agreement with the textures measured by X-ray. That is, there are mostly green and blue colors in about equal proportions in the A1 and C2 samples, which correspond to the orientations between $(10\bar{1}0)$ and $(2\bar{1}\bar{1}0)$ (see the color code triangle in Fig. 7). Those grains belong to fibers with the axis of the fiber lying in the ED–ND plane with the c -axis being the fiber axis. This is in accordance with the conclusion drawn from the pole figures and the ODFs. Even after deformation, the texture

remains a fiber in routes A and C, with the fiber axis in the ED–ND plane.

The situation is different for route B_c processed materials. The orientation map for the B2 sample (Fig. 6) shows many grains oriented corresponding to the red color, which means that the c -axes of those grains are nearly parallel to the TD axis of the specimen. This is due to the rotation of $+90^\circ$ applied around the specimen longitudinal axis necessary in route B_c, which brings the axis of the fiber texture nearly parallel to the TD direction; as shown in the pole figures (Fig. 6). Although the fiber axis moves towards the ideal B fiber, it remains $\sim 25^\circ$ from it. That is, many grains will be nearly TD axis oriented due to the very significant spread of orientations around the fiber. The proportion of the red colored grains in the EBSD-generated micrographs of the route B_c processed sample (B2) in Fig. 7 appears to be in accordance with the number of orientations expected in TD position.

An interesting feature of the grain structure in Fig. 7 is that the larger size grains are almost all green in color. These are grains with their $(2\bar{1}\bar{1}0)$ direction parallel to axis 3 of the specimen (the TD axis). This observation might be an indication of the occurrence of some selective dynamic recrystallization process, meaning that grains with such orientation recrystallize more slowly than other orientations. It is not excluded, then, that the large green grains originate from the initial grain structure.

6.6. Texture simulations

The results of the textures simulated using the viscoplastic polycrystal self consistent model are displayed in Figs. 4–6 for each of the corresponding experimental textures. In general, these textures are very similar to the experiments, as they reproduce the main features of the textures that were discussed in the above sections. Two techniques were applied in the simulations – one-pass and continuous simulations – see Section 5 above. It can be seen that the textures simulated from the previous experimental texture one pass are less strong than those obtained using the simulated textures. This is quite natural as there is certainly a significant grain refinement process together with important lattice curvatures within the grains in the present ECAE experiments [27,28], which is disregarded in the simulations. The refinement produces many subgrains in a grain that have slightly different orientations than the parent grain, leading to a smoothening of the texture. This feature is partly captured by the one-pass simulation technique, but completely disregarded in the continuous method. Nevertheless, seeing the quite good success of the textures simulated by both methods, we can say that the grain refinement process does not influence the textures in a very significant way.

It is quite a significant observation that the polycrystal model was able to reproduce the textures in spite of the fact that it did not contain any DRX modeling. This cannot be just a coincidence; this result must give information about the DRX process itself. Indeed, the DRX process in several hexagonal materials is a nucleation and growth of grains at $\pm 30^\circ$ around the c -axis of the crystal structure [29–32]. This rotation does not change the orientation of the c -axis. It was found in the present study that all deformation textures were fiber textures with the c -axis as the axis of the fiber. This means that newly oriented grains remained in the same fiber, but they appeared at another ϕ_2 location in the ODF. Consequently, the same kind of fiber persists due to such a DRX process. Nevertheless, a careful comparison of the fiber intensity distributions in the experimental and simulated (10 $\bar{1}$ 0) pole figures reveals that the intensity of the experimental fiber is more even than the simulated one. This again can be attributed to the occurrence of a $\pm 30^\circ$ c -rotation-DRX process, which would have a tendency to randomize the grain orientations along the c -fiber.

7. Conclusions

The textures that develop during ECAE of polycrystalline Mg have been studied in routes A, B_c and C up to four passes, both experimentally and by simulation. For the interpretation of the texture development, the ideal orientations and the rotation field were presented for the 90° ECAE process using the simple shear model. Our analysis has led to the following main conclusions.

1. There are very large lattice rotations during ECAE of Mg in routes A and C that can be twice as high as the imposed rigid-body rotation of the process. This feature, together with the rotation field characteristics of the process, provides a detailed explanation of the texture development. Route B_c is distinct as the texture rotates by a much smaller amount.
2. The qualitative agreement of the simulated textures with experimental textures indicates that the grain refinement process during ECAE of Mg does not dramatically alter the texture.
3. The textures that developed in ECAE of Mg were successfully reproduced by the VPSC model without considering DRX, which, however, took place during the tests. This result can be explained with a mechanism of DRX during which the newly formed grains are only rotated around the c -axis, so they remain in the c -fibers in the present study.

Acknowledgements

Satyam Suwas is grateful to Prof. Dr. G. Gottstein, Institut für Metallkunde und Metallphysik, RWTH, Aachen, Germany, for providing the texture measurement facility. The X-ray texture measurement experiments were carried out during his research stay as a Humboldt Fellow, for which he acknowledges financial support from the Alexander von Humboldt foundation. He is also thankful to Somjeet Biswas and Nilesh Gurao (IISc, Bangalore) for their help in EBSD experiments. This work was partially funded by the Natural Sciences and Engineering Research Council of Canada (NSERC). Kenneth Neale is Canada Research Chair in Advanced Engineered Material Systems and the support of this program is gratefully acknowledged.

Appendix A

In this Appendix, the lattice rotations are examined along the B fiber as well as along location defined by a $\varphi_1 = 90^\circ$ rotation of the B fiber. While the B fiber is a fiber of ideal orientations of simple shear textures, the orientations along the $\varphi_1 = 90^\circ$, $\varphi = 90^\circ$, $\varphi_2 = 0\text{--}60^\circ$ line are completely unstable. For simplicity, slip is supposed to be rate insensitive in the present calculation. Nevertheless, the results obtained can be readily transposed to the rate-sensitive case, as $m = 0$ is the limiting solution for strain-rate-sensitive slip. All equations will be written in the sample reference system.

First we examine the situation along the B fiber.

One can see from the definition of the B fiber ($\varphi_1 = 0^\circ$, $\varphi = 90^\circ$, $\varphi_2 = 0\text{--}60^\circ$) that the shear plane is parallel to the basal plane and there are three basal slip systems potentially active (see Fig. A1). The direction and the plane of the imposed simple shear are shown by the large arrow in Fig. A1. In the sample reference systems, the slip systems are defined by the slip directions $\underline{b}^{(s)}$ and the normal direction of the shear plane $\underline{n}^{(s)}$ as follows:

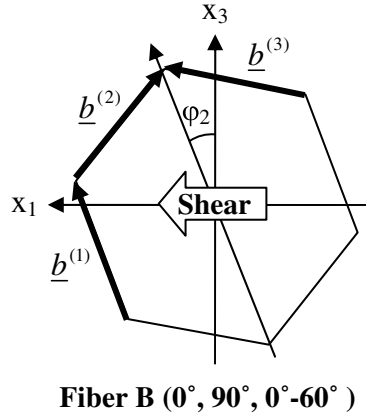


Fig. A1. The position of the three basal slip systems with respect to the applied simple shear along the B fiber.

$$\begin{aligned}
 \underline{b}^{(1)} &= (\sin \varphi_2, 0, \cos \varphi_2), \\
 \underline{b}^{(2)} &= (-\cos(\varphi_2 + \pi/6), 0, \sin(\varphi_2 + \pi/6)), \\
 \underline{b}^{(3)} &= (\cos(\pi/6 - \varphi_2), 0, \sin(\pi/6 - \varphi_2)), \\
 \underline{n}^{(1)} &= \underline{n}^{(2)} = \underline{n}^{(3)} = (0, 1, 0)
 \end{aligned} \quad (1)$$

The corresponding Schmid orientation matrices, defined by $m_{ij}^{(s)} = b_i^{(s)} n_j^{(s)}$, are:

$$\begin{aligned}
 \underline{m}^{(1)} &= \begin{pmatrix} 0 & \sin \varphi_2 & 0 \\ 0 & 0 & 0 \\ 0 & \cos \varphi_2 & 0 \end{pmatrix}, \\
 \underline{m}^{(2)} &= \begin{pmatrix} 0 & -\cos(\varphi_2 + \pi/6) & 0 \\ 0 & 0 & 0 \\ 0 & -\sin(\varphi_2 + \pi/6) & 0 \end{pmatrix}, \\
 \underline{m}^{(3)} &= \begin{pmatrix} 0 & \cos(\pi/6 - \varphi_2) & 0 \\ 0 & 0 & 0 \\ 0 & \sin(\pi/6 - \varphi_2) & 0 \end{pmatrix}.
 \end{aligned} \quad (2)$$

The imposed simple shear velocity gradient is:

$$\underline{L} = \begin{bmatrix} 0 & \dot{\gamma} & 0 \\ 0 & 0 & 0 \\ 0 & 0 & 0 \end{bmatrix}. \quad (3)$$

The strain rate tensor is obtained from \underline{L} as its symmetrical component:

$$\dot{\epsilon}_{ij} = \begin{bmatrix} 0 & \dot{\gamma}/2 & 0 \\ \dot{\gamma}/2 & 0 & 0 \\ 0 & 0 & 0 \end{bmatrix}. \quad (4)$$

Finally, the rigid body spin is defined by:

$$\beta_{ij} = \begin{bmatrix} 0 & \dot{\gamma}/2 & 0 \\ -\dot{\gamma}/2 & 0 & 0 \\ 0 & 0 & 0 \end{bmatrix}. \quad (5)$$

The slip rate can be obtained by solving the equation written for the strain rate:

$$\dot{\epsilon}_{ij} = \frac{L_{ij} + L_{ji}}{2} = \sum_{s=1}^3 \frac{1}{2} (m_{ij}^{(s)} + m_{ji}^{(s)}) \dot{\gamma}^{(s)}. \quad (6)$$

The above relation is reduced to only two independent equations, where $\dot{\gamma}^{(1)}$, $\dot{\gamma}^{(2)}$, and $\dot{\gamma}^{(3)}$ are the slip rates in the slip systems defined above:

$$\begin{aligned}
 \dot{\epsilon}_{12} = \frac{\dot{\gamma}}{2} &= \frac{1}{2} \dot{\gamma}^{(1)} \sin(\varphi_2) - \frac{1}{2} \dot{\gamma}^{(2)} \cos(\varphi_2 + \pi/6) \\
 &\quad + \frac{1}{2} \dot{\gamma}^{(3)} \cos(\pi/6 - \varphi_2),
 \end{aligned} \quad (7)$$

$$\begin{aligned}
 \dot{\epsilon}_{32} = 0 &= \dot{\gamma}^{(1)} \cos(\varphi_2) + \dot{\gamma}^{(2)} \sin(\varphi_2 + \pi/6) \\
 &\quad + \dot{\gamma}^{(3)} \sin(\pi/6 - \varphi_2).
 \end{aligned} \quad (8)$$

The above slip system cannot be solved uniquely as there are three unknowns for two equations. It can be readily seen, however, that not all three systems need to be activated for the imposed deformation. It can be seen from Fig. A1 that when $\varphi_2 = 0$, slip system no. 1 cannot be active as it is perpendicular to the imposed shear stress. This situation leads to the result that in the interval $0 \leq \varphi_2 \leq \pi/6$ there is double slip using systems 2 and 3. This situation will be called Case no. 1. Similarly, for the range of orientations $\pi/3 \leq \varphi_2 \leq \pi/6$, the active slip systems are nos. 2 and 3, which will be called Case no. 2. From Eqs. (7) and (8), the slip rates can be readily obtained for the double-slip case. Thus, for Case 1, the following slip distribution is obtained:

$$\begin{aligned}
 \dot{\gamma}^{(1)} &= 0, \quad \dot{\gamma}^{(2)} = -\dot{\gamma}^{(3)} \frac{\sin(\pi/6 - \varphi_2)}{\sin(\varphi_2 + \pi/6)}, \\
 \dot{\gamma}^{(3)} &= \dot{\gamma} \left(\frac{\sin(\pi/6 - \varphi_2)}{\tan(\varphi_2 + \pi/6)} + \cos(\pi/6 - \varphi_2) \right)^{-1}.
 \end{aligned} \quad (9)$$

Similarly, for Case 2, the solution is:

$$\begin{aligned}
 \dot{\gamma}^{(1)} &= -\dot{\gamma}^{(3)} \frac{\sin(\pi/6 - \varphi_2)}{\cos(\varphi_2)}, \quad \dot{\gamma}^{(2)} = 0, \\
 \dot{\gamma}^{(3)} &= \dot{\gamma} (\cos(\pi/6 - \varphi_2) - \sin(\pi/6 - \varphi_2) \tan(\varphi_2))^{-1}.
 \end{aligned} \quad (10)$$

The obtained slip distributions are displayed in Fig. A2. Now the velocity gradient corresponding to slip only (\underline{L}^g) is obtained using the results from Eqs. (9) and (10), over the whole interval of φ_2 (i.e. for Cases 1 and 2 simultaneously):

$$\underline{L}_{ij}^g = \sum_s m_{ij}^{(s)} \dot{\gamma}^{(s)} = \begin{bmatrix} 0 & \dot{\gamma} & 0 \\ 0 & 0 & 0 \\ 0 & 0 & 0 \end{bmatrix}. \quad (11)$$

The lattice rotation rate is defined as the difference between the macroscopic velocity gradient (Eq. (3)) and the plastic-slip defined velocity gradient (Eq. (11)) (see Ref. [21]):

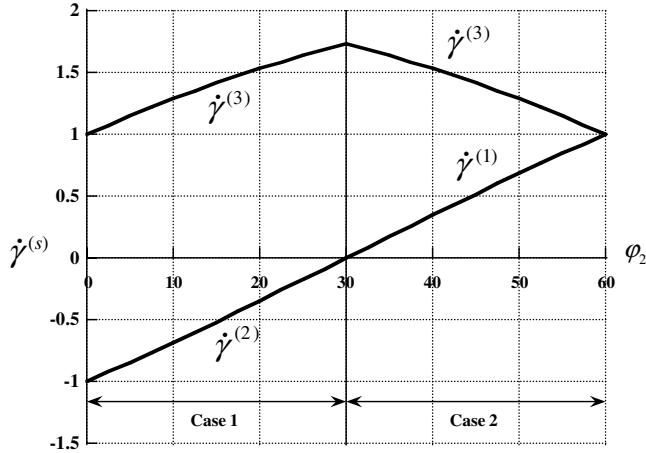


Fig. A2. The slip rates in the operating slip systems along the B fiber for an imposed shear rate of $\dot{\gamma} = \sqrt{3}$ [s⁻¹].

$$\dot{\Omega}_{ij} = L_{ij} - L_{ij}^g = \begin{bmatrix} 0 & \dot{\gamma} & 0 \\ 0 & 0 & 0 \\ 0 & 0 & 0 \end{bmatrix} - \begin{bmatrix} 0 & \dot{\gamma} & 0 \\ 0 & 0 & 0 \\ 0 & 0 & 0 \end{bmatrix} = 0. \quad (12)$$

Thus, as expected, the lattice rotation rate is zero along the ideal B fiber.

Now the case of the $\varphi_1 = 90^\circ$ rotated B fiber will be examined.

Along the rotated B fiber ($90^\circ, 90^\circ, 0-60^\circ$), the shear plane is not parallel to the basal plane; it is perpendicular to it, as shown in Fig. A3. The direction and the plane of shear are indicated by the two arrows in Fig. A3. The slip systems are defined by the slip directions $\underline{b}^{(s)}$ and the normal direction of the shear plane $\underline{n}^{(s)}$ as follows:

$$\begin{aligned} \underline{b}^{(1)} &= (0, -\sin \varphi_2, \cos \varphi_2), \\ \underline{b}^{(2)} &= (0, \cos(\varphi_2 + \pi/6), \sin(\varphi_2 + \pi/6)), \\ \underline{b}^{(3)} &= (0, -\cos(\pi/6 - \varphi_2), \sin(\pi/6 - \varphi_2)), \\ \underline{n}^{(1)} &= \underline{n}^{(2)} = \underline{n}^{(3)} = (1, 0, 0). \end{aligned} \quad (13)$$

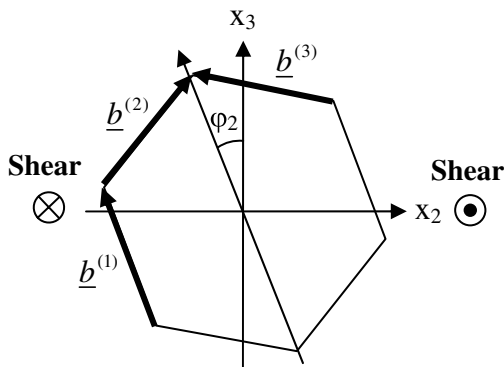


Fig. A3. Slip geometry along the 90° φ_1 -rotated B fiber.

The corresponding Schmid orientation matrices are:

$$\begin{aligned} \underline{m}^{(1)} &= \begin{pmatrix} 0 & 0 & 0 \\ -\sin \varphi_2 & 0 & 0 \\ \cos \varphi_2 & 0 & 0 \end{pmatrix}, \\ \underline{m}^{(2)} &= \begin{pmatrix} 0 & 0 & 0 \\ \cos(\varphi_2 + \pi/6) & 0 & 0 \\ \sin(\varphi_2 + \pi/6) & 0 & 0 \end{pmatrix}, \\ \underline{m}^{(3)} &= \begin{pmatrix} 0 & 0 & 0 \\ -\cos(\pi/6 - \varphi_2) & 0 & 0 \\ \sin(\pi/6 - \varphi_2) & 0 & 0 \end{pmatrix}. \end{aligned} \quad (14)$$

Using Eq. (6), the following two equations can be set up:

$$\begin{aligned} \dot{\epsilon}_{21} = \dot{\gamma} &= -\frac{1}{2}\dot{\gamma}^{(1)} \sin(\varphi_2) + \frac{1}{2}\dot{\gamma}^{(2)} \cos(\varphi_2 + \pi/6) \\ &\quad - \frac{1}{2}\dot{\gamma}^{(3)} \cos(\pi/6 - \varphi_2), \end{aligned} \quad (15)$$

$$\begin{aligned} \dot{\epsilon}_{31} = 0 &= \dot{\gamma}^{(1)} \cos(\varphi_2) + \dot{\gamma}^{(2)} \sin(\varphi_2 + \pi/6) \\ &\quad + \dot{\gamma}^{(3)} \sin(\pi/6 - \varphi_2). \end{aligned} \quad (16)$$

It is necessary to distinguish two cases again: $0 \leq \varphi_2 \leq \pi/6$ and $\pi/6 \leq \varphi_2 \leq \pi/3$. For the first case $0 \leq \varphi_2 \leq \pi/6$, we obtain with a similar analysis as for the B fiber, that the active slip systems are $\dot{\gamma}^{(2)}$ and $\dot{\gamma}^{(3)}$. By solving Eqs. (15) and (16) we obtain the slip distribution:

$$\begin{aligned} \dot{\gamma}^{(1)} &= 0, \\ \dot{\gamma}^{(2)} &= \dot{\gamma} \left(\frac{\sin(\pi/6 + \varphi_2)}{\tan(\pi/6 - \varphi_2)} + \cos(\pi/6 + \varphi_2) \right)^{-1}, \\ \dot{\gamma}^{(3)} &= -\dot{\gamma}^{(2)} \frac{\sin(\pi/6 + \varphi_2)}{\sin(\pi/6 - \varphi_2)}. \end{aligned} \quad (17)$$

For the second case $\pi/3 \leq \varphi_2 \leq \pi/6$, the active slip systems are $\dot{\gamma}^{(1)}$ and $\dot{\gamma}^{(3)}$, and the solutions are:

$$\begin{aligned} \dot{\gamma}^{(1)} &= \dot{\gamma} \left(\frac{\cos(\varphi_2)}{\tan(\pi/6 - \varphi_2)} - \sin(\varphi_2) \right)^{-1}, \\ \dot{\gamma}^{(2)} &= 0, \quad \dot{\gamma}^{(3)} = -\dot{\gamma}^{(1)} \frac{\cos(\varphi_2)}{\sin(\pi/6 - \varphi_2)}. \end{aligned} \quad (18)$$

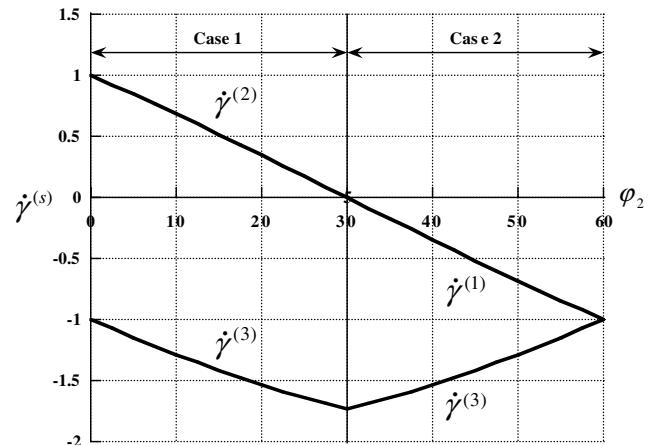


Fig. A4. Slip distribution along the 90° φ_1 -rotated B fiber.

The obtained slip distribution for the two intervals is displayed in Fig. A4. As can be seen, the slips are exactly the opposite for the present 90° rotated B-fiber as compared to Fig. A2.

Now the velocity gradient corresponding to plastic slip only \underline{L}^g is obtained from Eqs. (15) and (16), which is identical for the two intervals:

$$L_{ij}^g = \sum_s^3 m_{ij}^{(s)} \dot{\gamma}^{(s)} = \begin{bmatrix} 0 & 0 & 0 \\ \dot{\gamma} & 0 & 0 \\ 0 & 0 & 0 \end{bmatrix}. \quad (19)$$

Finally, the lattice rotation rate is obtained:

$$\begin{aligned} \dot{\Omega}_{ij} &= L_{ij} - \sum_s^3 m_{ij}^{(s)} \dot{\gamma}^{(s)} = \begin{bmatrix} 0 & \dot{\gamma} & 0 \\ 0 & 0 & 0 \\ 0 & 0 & 0 \end{bmatrix} - \begin{bmatrix} 0 & 0 & 0 \\ \dot{\gamma} & 0 & 0 \\ 0 & 0 & 0 \end{bmatrix} \\ &= \begin{bmatrix} 0 & \dot{\gamma} & 0 \\ -\dot{\gamma} & 0 & 0 \\ 0 & 0 & 0 \end{bmatrix} = 2\dot{\beta}_{ij}. \end{aligned} \quad (20)$$

Thus, along the 90° rotated B fiber, the lattice rotation rate is twice as high as the rigid body rotation rate.

Appendix B. Supplementary material

Supplementary data associated with this article can be found, in the online version, at doi:10.1016/j.actamat.2007.09.032.

References

- [1] Agnew SR, Duygulu O. *Int J Plasticity* 2005;1161:1193.
- [2] Agnew SR, Horton JA, Lillo TM, Brown DW. *Scripta Mater* 2004;377:381.
- [3] Agnew SR, Mehrotra P, Lillo TM, Stoica GM, Liaw PK. *Acta Mater* 2005;3135:3146.
- [4] Agnew SR, Mehrotra P, Lillo TM, Stoica GM, Liaw PK. *Mater Sci Eng A* 2005;72:78.
- [5] Mehrotra P, Lillo TM, Agnew SR. *Scripta Mater* 2006;855:858.
- [6] Agnew SR, Brown DW, Tome CN. *Acta Mater* 2006;4841:4852.
- [7] Suwas S, Gottstein G, Kumar R. *Mater Sci Eng A* 2007;1:14.
- [8] Gehrmann R, Frommert M, Gottstein G. *Mater Sci Eng A* 2005;339:349.
- [9] Furui M, Kitamura H, Anada H, Langdon TG. *Acta Mater* 2007;1083:1091.
- [10] Figueiredo RB, Langdon TG. *Mater Sci Eng A* 2006;151:156.
- [11] Estrin Y, Hellmig RJ, Ek MJ, Lamark TT, Zúberová Z, Lapovok R, et al. *TMS Annu Meet* 2006;381:388.
- [12] Kim WJ, Sa YK. *Scripta Mater* 2006;1391:1395.
- [13] Beausir B, Tóth LS, Neale KW. *Acta Mater* 2007;2695:2705.
- [14] Segal VM. *Mater Sci Eng A* 1999;322:333.
- [15] Tóth LS, Arruffat Massion R, Germain L, Baik SC, Suwas S. *Acta Mater* 2003;1885:1898.
- [16] Beyerlein IJ, Tomé CN. *Mater Sci Eng A* 2004;171:190.
- [17] Mathieu JP, Suwas S, Eberhardt A, Tóth LS, Moll P. *J Mater Process Technol* 2006;29:33.
- [18] Molinari A, Canova GR, Ahzi S. *Acta Metall* 1987;2983:2994.
- [19] Molinari A, Tóth LS. *Acta Metall Mater* 1994;2453:2458.
- [20] Hutchinson JW. *Proc Roy Soc Lond A* 1976;101:127.
- [21] Asaro RJ, Needleman A. *Acta Metall* 1985;923:953.
- [22] Tóth LS, Gilormini P, Jonas JJ. *Acta Metall* 1988;3077:3091.
- [23] Neale KW, Tóth LS, Jonas JJ. *Int J Plasticity* 1990;45:62.
- [24] Van der Giessen E, Wu PD, Neale KW. *Int J Plasticity* 1992;773:801.
- [25] Clément A, Coulomb P. *Scripta Metall* 1979;899:901.
- [26] Gilormini P, Tóth LS, Jonas JJ. *Proc Roy Soc Lond* 1990;489:507.
- [27] Jin L, Lin D, Mao D, Zeng X, Chen B, Ding W. *Mater Sci Eng A* 2006;247:252.
- [28] Yamashita A, Horita Z, Langdon TG. *Mater Sci Eng A* 2000;142:147.
- [29] Galiyev A, Kaibyshev R, Gottstein G. *Acta Mater* 2001;1199:1207.
- [30] Tan JC, Tan MJ. *Mater Sci Eng A* 2002;124:132.
- [31] YI SB, Zaefferer S, Brokmeier HG. *Mater Sci Eng A* 2006;275:281.
- [32] Fatemi-Varzaneh SM, Zarei-Hanzaki A, Beladi H. *Mater Sci Eng A* 2007;52:57.